Dielectric Barrier Discharge Plasma Flow Control on a Vertical Axis Wind Turbine

David Greenblatt, Hanns Müller-Vahl, Ronen Lautman,
Amos Ben-Harav, and Ben Eshel

Faculty of Mechanical Engineering,
Technion, Israel Institute of Technology, Technion City, Haifa 32000, Israel

Abstract. Unsteady flow separation was partially controlled on a double-bladed H-Rotor vertical axis wind turbine model using pulsed dielectric barrier discharge plasma actuators at wind speeds between 4.4m/s and 7.1m/s. With pulsations applied in an open-loop manner on the inboard side of the blades, flowfield measurements showed that the development and shedding of the dynamic stall vortex could be modified. Pulsations were then applied in a feed-forward manner by predetermining the plasma-pulsation initiation and termination azimuth angles. These angles were selected on the basis of wind speed and turbine rotational speed, with the objective of maximizing the net turbine output power. Remarkably, a net turbine power increase of more than 10% was measured. For the purposes of power regulation, a hysteresis controller was applied to the turbine subjected to a fluctuating wind profile. Control produced a 7% increase in net power and a reduction from ±6.5% to ±1.3% in power fluctuations.

1 Introduction

Wind energy is the fastest-growing renewable energy resource, with an average increase of 28% in new installations each year. In addition to the development of multi-megawatt wind farms, significant resources are being channeled to off-grid or feed-in small wind turbines (SWTs; ≤100 kilowatts). Recent demand has driven renewed interest in vertical axis wind turbines (VAWTs) [1-8] due to their insensitivity to wind direction, proximity of the generator to the ground and relatively low noise levels. Furthermore, blade profile uniformity along the span can significantly reduce manufacturing costs. A drawback of VAWTs is the dynamic stall [9] their blades experience as they are pitched beyond their static stall angle [10,11]. This has several undesirable effects: there is a sharp drop in blade lift, producing large power fluctuations and large unsteady loads are imposed on the generator and drive train [12]. In many cases the problem is compounded in built-up areas or on buildings where VAWTs are often required to operate in highly unsteady winds and at low rotational speeds. This forces the turbine to operate in a partially stalled state that is exacerbated at high wind-speed when the potential for power generation is maximized.

R. King (ed.), *Active Flow and Combustion Control 2014*, Notes on Numerical Fluid Mechanics and Multidisciplinary Design 127, DOI: 10.1007/978-3-319-11967-0_5

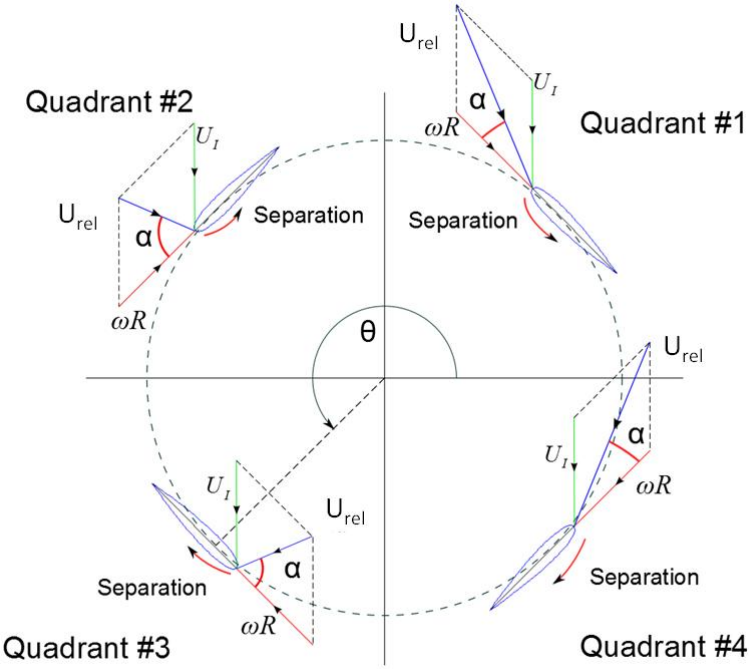

Fig. 1. Top view schematic of a hypothetical four-bladed VAWT showing the velocity components relative to the blade depending upon the position of the blade

The control of unsteady separation, also known as dynamic stall, on airfoils has been achieved by means of introducing periodic perturbations such as zero mass-flux blowing [13-16] and dielectric barrier discharge (DBD) plasma actuation [17]. Recently, our group manipulated dynamic stall on the blades of a small high-solidity vertical axis wind turbine by means of DBD plasma actuators installed on the blade leading-edges [18,19]. A parametric study was conducted to assess the effects of non-dimensional frequency and duty cycle, with the objective of increasing the net power output resulting from control in an open-loop manner. Actuators were configured to control separation on the upwind half of the turbine azimuth and wind speeds in the range 4.4m/s to 7.1m/s were considered. Dynamic stall on VAWTs is unique in that it occurs alternately on the inboard or the outboard surfaces of the blades depending on whether they are upwind or downwind. A schematic showing an idealized VAWT plan view in fig. 1 illustrates the differences between inboard and outboard dynamic stall. Here U_I is the wind velocity immediately upwind of the turbine, U_{rel} is the velocity relative to the blade and α is the local instantaneous angle of attack. The curved arrows indicate dynamic stall occurring on the inboard surface of the blade when the blade is in the upwind half of the azimuth (quadrants #1 and #2). Likewise, the curved arrows indicate dynamic stall occurring on the outboard surface when the blade is in the downwind half of the azimuth (quadrants #3 and #4).

The objective of this paper is to demonstrate a closed-loop control scheme applied to a VAWT. Initially Particle Image Velocimetry (PIV) data were acquired to determine the physical mechanism of control. Following this, a feed-forward controller was developed to initiate and terminate plasma actuation at predetermined initiation and termination angles, θ_i and θ_t. With this controller, plasma pulsation frequency and pulsation duty cycle were varied systematically to maximize turbine performance. Finally, a simple feedback hysteresis control scheme (on–off controller) was employed to increase the net power output and regulate power fluctuations.

2 Experimental Setup

The turbine employed in this investigation (see fig. 2) was an H-rotor (diameter D=0.5m and height H=0.6m) with two composite NACA 0015 blades (chord length c=0.15m) connected to a vertical shaft by means of horizontal adapters. The setup, described in detail in [18], was inverted such that the upper blade tip was closely aligned with the upper adapter. This formed a 25cm (1.67c) free end below the lower adapter (fig. 2a) to facilitate PIV measurements midway between the adapter and the blade-tip. This location was considered to be sufficiently far from both the adapter and the blade-tip so as to be representative of the turbine blade flowfield (see section 3 below). The turbine was installed in a low-speed wind tunnel (dimensions 1.0m× 0.61m×2.0m) with a maximum speed (U_∞) of 55m/s and maximum turbulence level

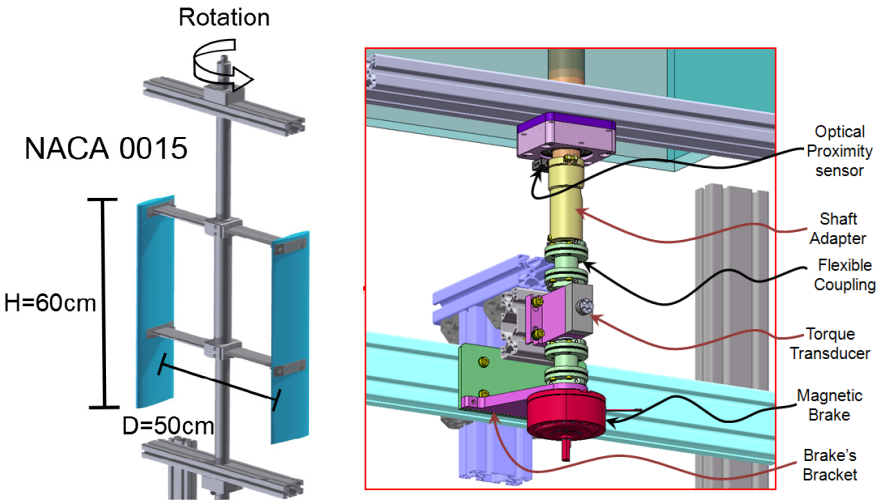

Fig. 2. (a) Schematic of the turbine mounted in the wind tunnel test section, showing the main dimensions; (b) Schematic of the custom-designed dynamometer with shaft adapter for the slip-ring (not shown)

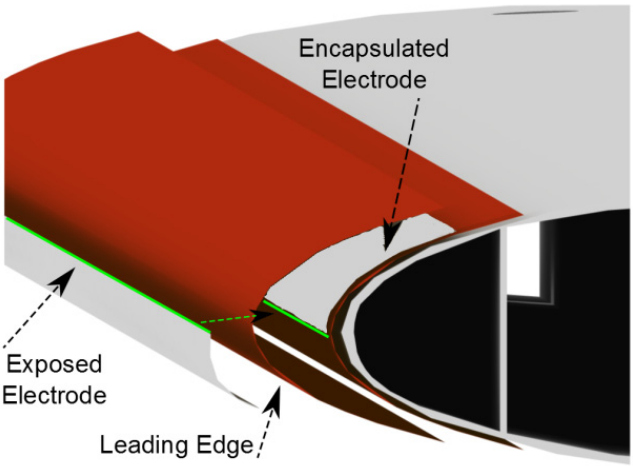

Fig. 3. Schematic of the DBD plasma actuators considered in this study showing the exposed and encapsulated electrode alignment at the leading-edge

of 0.1% relative to the free-stream velocity. The tunnel velocity was monitored by means of a Pitot-static probe, mounted immediately upstream of the turbine. Turbine power P was measured by means of a dynamometer, comprising a Magtrol Magnetic Brake (1.4Nm maximum; Coulomb damping) and a Kistler torque/rotational speed transducer (maximum nominal torque T of $1.56\text{Nm} \pm 0.2\%\text{FSO}$) and flexible couplings (see fig. 2b).

Asymmetric DBD plasma actuator configurations, which are commonly-used for flow control applications [17,20], were deployed at the leading-edges of the blades (fig. 3). They consisted of 70µm thick exposed and encapsulated electrodes that were separated by 125µm of Kapton© polyimide tape and aligned with the leading-edge. Each actuator was configured to act inboard on the blades and was thus only active on the upwind half of the turbine. Plasma was generated using two Minipuls high-voltage inverters (GBS Elektronik) that require a dc voltage (V_{in}) and current (I_{in}) input, thereby facilitating simple calculation of the gross power supplied to the actuation system ($P_{in}=V_{in}I_{in}$). Note that this was not the power dissipated in the actuators. Signals of 8kVpp at f_{ion}=8kHz were used to generate the plasma, as these produced the smallest harmonic content, and these were pulsed at $f_p = 500\text{Hz}$ with duty cycles (DC) of between 1% and 20%. This f_{ion} and f_p combination thus produced truncated pulsation cycles; the consequences of this are discussed in section 4. Slip-rings were used at both ends of the shaft to transfer the high-voltage stationary ac signal to the rotating system and these are described in detail in [17].

The PIV data were acquired with a 200 mJ double-pulsed Nd-YAG laser and a 4 megapixel CCD camera. The laser light sheet was oriented horizontally and perpendicular to the blade plane at a spanwise distance of $0.83c$ from both the adapter and the blade free edge (see fig. 1a). A seeding generator, producing particles 1µm diameter, was placed upstream of the wind tunnel inlet. Sufficient seeding density to produce

high-quality PIV measurements was achieved by filling the entire laboratory space with seeding particles. A mirror was placed beneath the test section at a 45° angle and the PIV camera was placed in front of the mirror. The use of the mirror was necessary to orient the camera axis horizontally and thereby avoid accumulation of seeding particles on the lens. 3M red reflective tape was placed on all aluminum components. In combination with a filter mounted in front of the camera lens that permits only light of the Nd-YAG laser (532nm) to be captured, this significantly reduced reflections and thereby improved the data quality. Additional details of the PIV setup can be found in [19].

3 Dynamic Stall Vortex Control

For all PIV data sets, 400 image pairs were acquired with a pulse separation of $\Delta t = 25\mu s$. The data were processed with a multi-pass algorithm using 64×64 pixel interrogation windows initially and 16×16 pixel windows for the final results. These measurements were made with the pulsed plasma operating continuously, thus we refer to this as open-loop control. The velocity component ωR resulting from the rotation of the blade was subsequently added to the velocity fields so as to present the data in the coordinates of a stationary blade. The vorticity distributions were calculated from the mean velocity fields and non-dimensionalized with respect to the chord length and the wind tunnel speed:

$$\omega_z = \left[\frac{\partial v}{\partial x} - \frac{\partial u}{\partial y} \right] \cdot \frac{c}{U_\infty} \tag{1}$$

Example PIV data sets for baseline and open-loop control cases recorded at $\theta = 120°$ (quadrant #2) are shown in figs. 4a and 4b respectively. Under baseline conditions, the initial tip speed ratio of $\lambda_0 \equiv \omega R / U_\infty = 1.37$ corresponds to an angle-of-attack of approximately 47° at this azimuthal position; hence this can be considered as very deep stall. Not surprisingly, the baseline PIV data shows a large dynamic stall vortex (DSV) in the process of being shed from the leading-edge on the inboard side of the blade (fig. 4a). In addition, a large region of vortical flow is present above the aft region of the blade. A similar phenomenon was observed by [21] on a pitching NACA 0018 airfoil and is believed to originate from trailing-edge separation on thick airfoils, particularly at low Reynolds numbers. A feature generally not observed on oscillating airfoils is the strong shear layer that forms at the trailing-edge. This is attributed to the small radius of the turbine relative to the chord length, c/R=0.6. After the baseline data had been recorded, the plasma pulsations were initiated with the brake torque left unchanged. As a result of control the turbine speed increased and PIV data was recorded once it had settled to new final steady state at $\lambda_F = 1.48$ (fig. 4b). With control the vortex is smaller and closer to the surface of the blade. Aft on the blade, the vortical region is stronger and the magnitude of the flow towards the surface is greater. These observations are consistent with the higher tip speed ratio and represent an

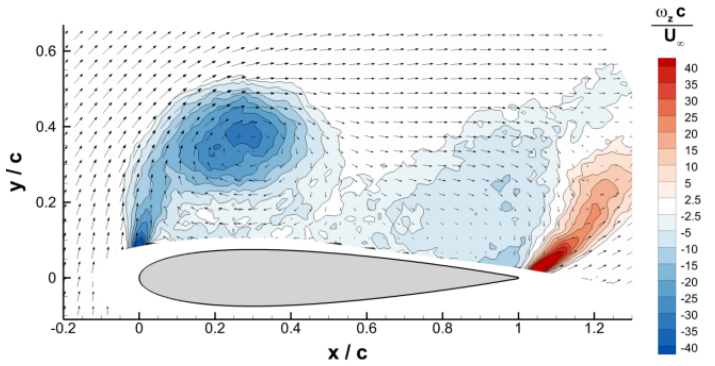

(a)

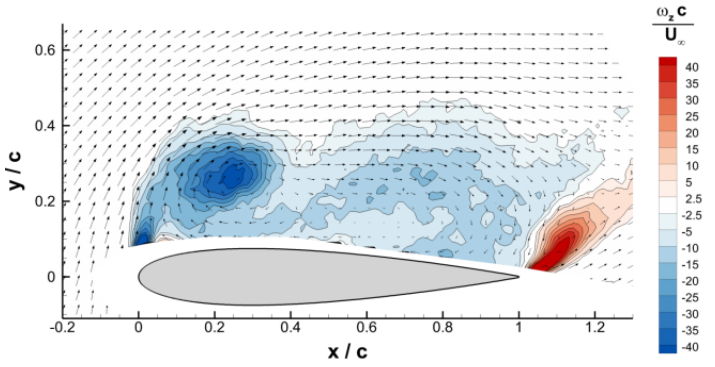

(b)

Fig. 4. Phase averaged velocity and vorticity fields recorded at $\theta = 120°$ with U_∞=7m/s showing (a) the baseline at $\lambda_0 = 1.37$ and (b) pulsed plasma at $\lambda = 1.48$. Pulsed plasma perturbations are at 500Hz and 20% duty cycle.

increase in measured power of 8%. It is evident from these data that the measured increases in turbine power result from a modification of the DSV and the aft flowfield.

Increasing the brake torque, and thereby returning the turbine to $\lambda = 1.37$ with plasma pulsations, resulted in a smaller visible effect on the DSV even though the power increased by 16.4%. The small effect was attributed to the exceedingly large maximum angle-of-attack (approximately 47°). A similar experiment, carried out at a lower brake setting with $\lambda_0 = 1.74$ and hence maximum angle-of-attack of 35°, produced a greater effect on the DSV [19] although elimination of dynamic stall was certainly not achieved. This is mainly due to low thrust produced by the actuators; indeed the maximum torque measured with the actuators alone is at most two orders of magnitude less than the measured changes. Nevertheless, in future investigations significantly greater control authority could be exerted over the vortex with larger amplitude pulsed-plasma perturbations [23].

4 Feed-Forward Control

The data presented in the previous section was acquired in an open-loop manner with the actuators operating continuously and, as such, the plasma pulsations and azimuthal angle were independent of one another. The purpose of the feed-forward control system developed here was to initiate and terminate plasma actuation at predetermined azimuthal angles θ. The system consisted of a wheel, two metallic clips and a proximity transducer (see fig. 5). The wheel was printed using Object Fullcure720® and incorporated an inner and outer circular ring of holes producing a discretization of 1°. The metallic clips could be located independently on the holes and were always located with a spacing of 180° relative to each other; the two-clip arrangement ensured a trigger for each blade, namely at θ_i and at $\theta_i + 180°$. The wheel was bolted to

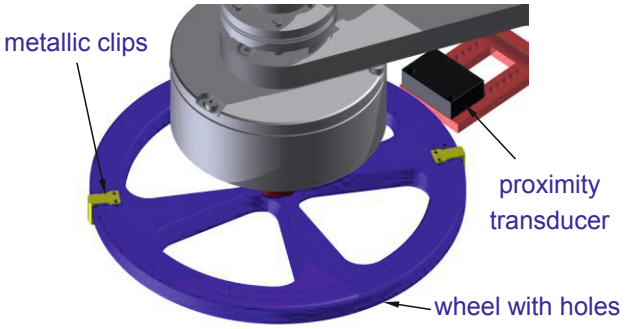

Fig. 5. Schematic of the wheel attached to the brake shaft with attached metallic clips. Sensing of clips by the proximity transducer triggers the pulsed-plasma initiation

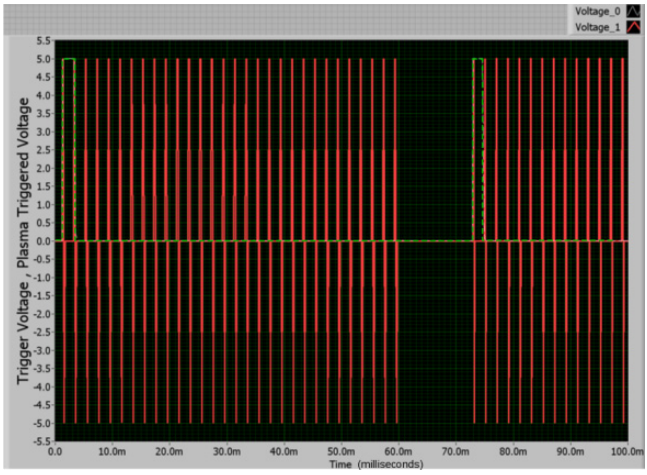

Fig. 6. LabVIEW screenshot showing synchronization of the trigger signal and pulsed plasma driving signal. (Green line represents the trigger; red lines represent the plasma pulses.)

the bottom brake shaft as shown in fig. 5. A bracket was mounted to the frame of the wind tunnel upon which a proximity transducer (TL-18 Series KFPS) was located. With this arrangement, arbitrary angles could be selected to trigger, or initiate, the plasma pulsations. For each trigger signal, a user defined number of plasma pulses N was generated where the frequency and duty cycle could be independently varied (see fig. 6). For the present experiments, these were maintained constant during each turbine transient. With the plasma initiation angle and the number of pulses predetermined, the termination angle was calculated according to:

$$\theta_t = \theta_i + \omega N / f_p \tag{2}$$

where ω is the measured turbine rotational speed. This facilitated the definition of the turbine duty cycle, namely:

$$DC_T = (\theta_t - \theta_i)/180° \tag{3}$$

where the angles are measured in degrees. The parameters on the right hand side of equation 2 were always chosen to ensure that $\theta_t < 180°$. Simultaneous measurements were made of the tunnel speed (Pitot-static probe), trigger signal, turbine torque and rotational speed, and plasma dc supply voltage and current (see section 2).

To determine the effect of initiation and termination angles, the following plasma excitation conditions were selected: 8kVpp, $f_p = 500$Hz and 20% duty cycle. Experiments were performed at tip speed ratios in the range $1.38 \le \lambda \le 1.53$. For each combination of θ_i and θ_t, after a steady state had been reached, the change in turbine rotational speed ΔRPM relative to the baseline was recorded. Initially, the metallic clips were located on the wheel to produce a plasma initiation angle of $\theta_i = 0°$. The number of plasma pulses was set to N=35 to give a termination angle θ_t slightly less than $180°$. N was then systematically reduced until N=5 and following this, the metallic clips were relocated to produce $\theta_i = 10°$. A starting N<35 was selected to ensure that $\theta_t < 180°$ and again reduced systematically. This process was repeated up to, and including, $\theta_i = 80°$, where performance increases were significantly smaller. A final data set was acquired with the clips at $\theta_i = 75°$.

A selection of data generated in this manner is summarized on the plot shown in fig. 7 where the standard deviation for a 95% confidence interval is displayed for a sample data set. The ΔRPM data are directly proportional to changes in turbine power $P_F - P_0 = T(\Delta\omega)$, where the subscripts refer to the "final" actuated and "initial (0)" baseline states, because the brake torque T was maintained constant. The graph shows a number of important results of feed-forward control. Starting with $0° \le \theta_i \le 30°$, when $\theta_t < 60°$ there is a small negative effect, namely the turbine speed reduces slightly ($\Delta\omega < 0$) when plasma is operating in the $0° < \theta < 60°$ range. The reason for this is not clear, but perhaps the perturbations cause mild separation when the flow is fully attached. This effect has been observed in flow control studies on airfoils with attached boundary layers, but using steady air jets [22]. Based on the data shown in [26], it is speculated that applying plasma actuation at 100% duty cycle may have a similar effect and could possibly be used for braking the turbine, but this was not investigated here.

More importantly for purposes of increasing performance, when perturbations are introduced at $40° \le \theta_i \le 70°$, there is always a positive result. Note, however, that the effect saturates at $\theta_t \approx 110°$. This is an important observation because it means that the additional pulsations at $\theta_t > 110°$, and therefore additional power supplied to the actuators, do not produce an additional increase in the turbine power. Increasing θ_i to 75° resulted in a smaller RPM increment than that measured with $\theta_i \approx 70°$ and this effect was even more pronounced for $\theta_i = 80°$. Overall, these results indicate optimum values of $\theta_i \approx 70°$ and $\theta_t \approx 110°$ since this combination produced the largest performance enhancement but only required the plasma to operate throughout a small azimuthal range. The corresponding range of angles of attack can be calculated as $\alpha = \tan^{-1}\left[\sin\theta / (\lambda + \cos\theta)\right]$ when the induced velocity upstream of the turbine is assumed to be equal to the wind tunnel velocity [19]. This approximation yields plasma initiation angles of attack significantly higher than the static stall angle, namely $23° \le \alpha \le 35°$.

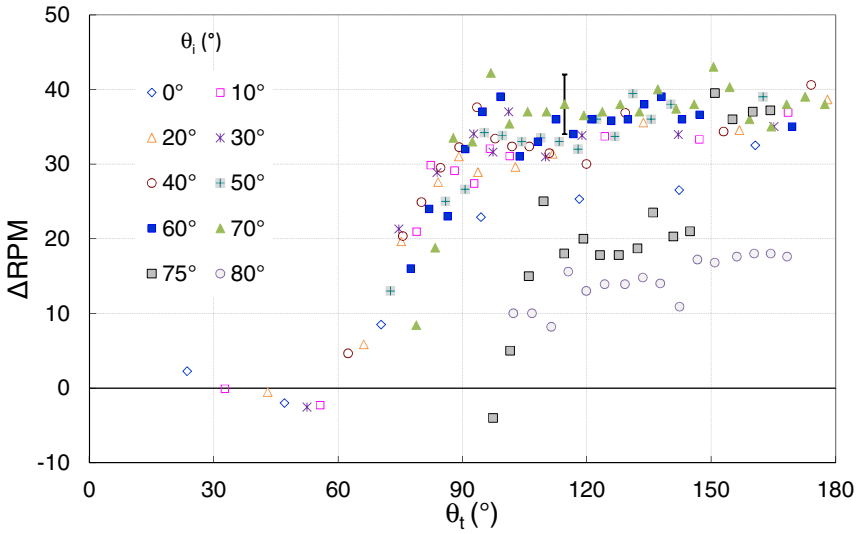

Fig. 7. Effect of azimuthal angle initiation and termination of pulsed plasma actuation: $0° \le \theta_i \le 80°$, $f_p = 500\text{Hz}$, 20% Duty Cycle, $U_\infty = 7\text{m/s}$, initial $\lambda_0 = 1.38$. Sample standard deviation bar shown for 95% confidence interval.

With the turbine duty cycle minimized, a systematic set of experiments was performed with a view to further reducing DC and P_{in}. In general, the measurement of power dissipated in the actuator requires additional electronics. Fortunately, the inverters employed here are supplied with a low-voltage dc source. Hence the power consumed by the actuators, including all losses, was calculated by the dc P_{in}=$V_{in}I_{in}$ as described in section 2.

This facilitated the calculation of maximum gross and net power changes produced by actuation which were calculated as percentages according to:

$$\Delta P_{\text{gross}} = [(P_F - P_0) / P_0] \times 100 \tag{4}$$

$$\Delta P_{\text{net}} = [(P_F - P_0 - P_{\text{in}}) / P_0] \times 100 \tag{5}$$

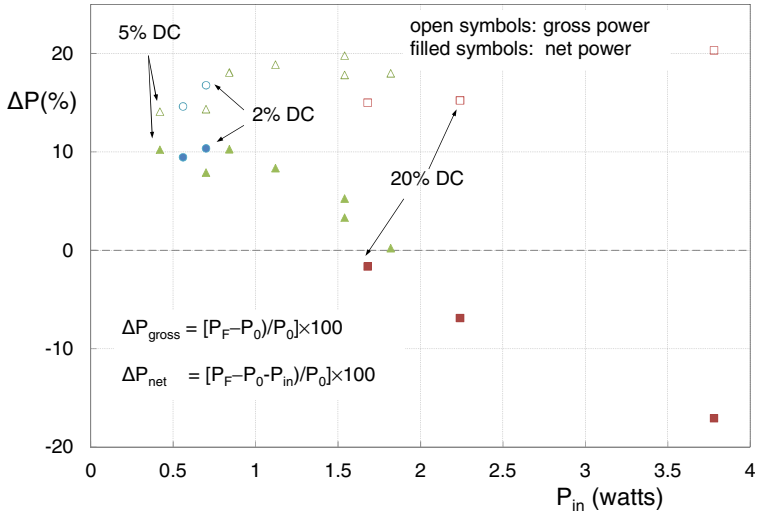

Fig. 8. Gross and net turbine power increase in percentage as a function actuator power. Actuation conditions: $\theta_i = 70°$; $U_\infty = 7\text{m/s}$; initial $\lambda_0 = 1.36$; $5.3 \le F^+ \le 7.3$

Results calculated according to equations 4 and 5 are presented in fig. 8 and are shown as a function of the power input to the actuators. The power varies mainly as result of the reduction the turbine duty cycle (corresponding to a reduction of *N*) while the different symbols represent different pulsation duty cycles. Open and filled symbols represent gross and net power output respectively. The gross change in power varies from 15% to 20% for these experiments. Note, however, that DC=20% does not produce a net turbine power increase but almost breaks even. For DC=2% and 5%, net positive turbine power is produced with comparable results of approximately 10% in both cases. Despite this positive result, the experiments were hampered by the combination of f_{ion}=8kHz (which produced the least harmonic content) and $f_p = 500\text{Hz}$ (which was the lowest viable pulsation frequency; see discussion below). This resulted in truncated pulsation cycles for all duty cycles used here, namely those that were not integer multiples of $f_p / f_{\text{ion}} \times 100 = 6.25$. An oscilloscope signal indicated that truncated signals, or a fraction of a cycle for DC<6.25%, resulted in the excitation of the inverter resonance that, for these experiments, was approximately 17kHz. Future experiments on this turbine will maintain full, non-truncated, cycles in order to establish an accurate representation of power consumption.

As alluded to above, and consistent with a previous open-loop investigation [18], the turbine performance was reduced with successive reductions in f_p. This was counterintuitive because the largest performance gains were recorded with reduced frequencies in the range of $5.3 \le F^+ \equiv f_p c / U_{\text{rel}} \le 7.3$ ($f_p = 500\text{Hz}$) even though the optimum value for separation control with periodic excitation is typically on the order of $F^+ \approx 2$ [14, 24]. It was speculated that by lowering f_p, too few plasma pulses were produced in the region where dynamic stall was occurring, namely in quadrants #1 and #2 identified in fig. 1. The number of pulses generated within the effective azimuth range can be estimated by substituting $\theta_i = 70°$ and $\theta_t = 110°$ in equation (2) and rearranging, to produce: $N = \mathbb{Z}(2\pi f_p / 9\omega)$. Pulsing the plasma actuators at $f_p = 500\text{Hz}$ gives $N = 9$, reducing the frequency to $F^+ = 2$ results in N values of 2 or 3 which appear to be insufficient to produce a meaningful effect on dynamic stall. However, with the turbine stationary, the largest changes to torque were observed at $F^+ \approx 2$; these changes were approximately twice as large as those observed with $5.3 \le F^+ \le 7.3$ [18]. This is in line with established findings on separation control, indicating that a larger performance enhancement could potentially be achieved if a sufficient number of plasma pulses could be generated at a lower reduced frequency within the effective azimuth range. The simplest way to overcome this problem is to increase the turbine radius. For example, increasing the radius by a factor of 4, namely to *R*=1m, would facilitate $N = 13$ at $F^+ \approx 2$ for a turbine operating at the same λ. Furthermore, with the present inverter, lower plasma duty cycles (≤1.5%) could be employed.

Without accounting for the power supplied to the actuation system, a comparison of feed-forward versus open-loop control showed the former to be superior by 7.5% to 12.0% depending on the control parameters. The reason for this relatively small difference was the large disparity between the pulsation frequency and turbine rotational frequency, namely $2\pi f_p / \omega = \text{O}(10^2)$. Therefore, due to the random nature of open-loop control, a similar but smaller number of pulsations were produced in the azimuth demarcated by $70° \le \theta \le 110°$.

5 Feedback Hysteresis Control

With power-efficient feed-forward control demonstrated, attention was focused on rudimentary feedback control, namely hysteresis (or on-off) control. The objective was to regulate the turbine's power when it was subjected to unsteady wind conditions. In contrast to feed-forward control that was applied within the azimuth of each rotation, feedback control was based on the integral rotational speed of the turbine. Thus both feed-forward and feedback control were applied simultaneously, with the former nested within the latter. Simulated unsteady wind conditions were generated by using a system of louver vanes mounted downstream of the turbine at the test section exit. The system consisted of 13 counter-rotating louvers and was driven by a 0.75 kW servo-motor with a 5:1 gear (see fig. 9a). The motor drove the vanes via the gear mechanism shown in fig. 9b thereby varying the exit area and consequently the head-loss, for details see [25].

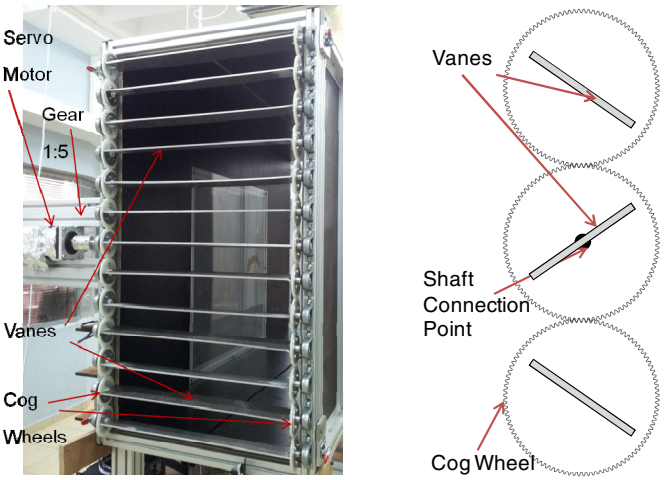

(a) (b)

Fig. 9. (a) Photograph of the louver mechanism attached to the wind tunnel exit, shown with the louvers fully open; (b) cross-section schematic of three vanes illustrating the gear mechanism

For all experiments performed, the tunnel wind speed was varied between approximately 6.05m/s and 6.60 m/s. Wind fluctuation periods between 20 seconds and 80 seconds were considered. For all experiments, the feed-forward parameters were employed as in section 4 with DC=20% and the feedback logic was as follows:

$$P_{out} - P_{set} < 0: \quad \text{actuation on}$$
$$P_{out} - P_{set} \geq 0: \quad \text{actuation off}$$

As in the previous section, the brake setting is maintained constant and thus changes to turbine RPM are directly proportional to the turbine power. Therefore, selecting P_{set} is equivalent to selecting RPM_{set}. This logic is shown in the block diagram of fig. 10. It also includes the nested feed-forward scheme which adapts θ_i and N to the unsteady operating conditions to maintain the optimum values derived in section 4. For purposes of illustration we show here wind fluctuation periods of 40 seconds together with measured turbine RPM in figs. 11a and 11b for baseline and controlled cases respectively. These data are also broadly consistent with those at lower and higher wind fluctuation frequencies. In the uncontrolled case, the wind turbine can be seen to "track" the wind speed fluctuations. This was expected because the turbine behaves like a non-linear first-order system with a time constant of approximately 10 seconds. It can be shown from fig. 11a that the relative changes to turbine power are larger than the relative changes in wind speed: ±4.3% fluctuations in wind speed result in ±6.5% fluctuations in power output.

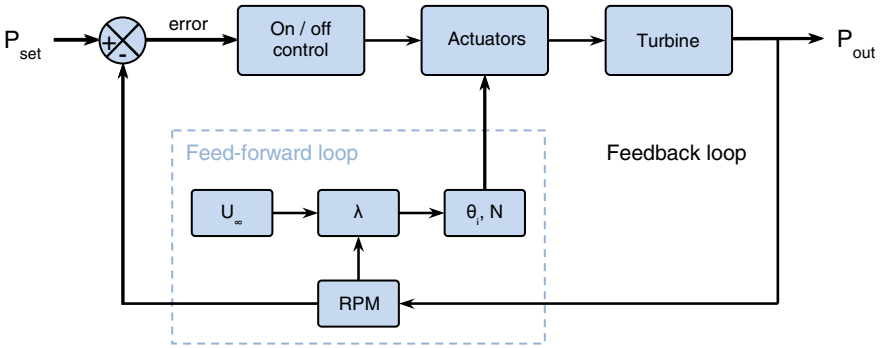

Fig. 10. Block diagram showing the feedback control scheme applied once per second. The nested feed-forward control was applied within the turbine azimuth or rotation.

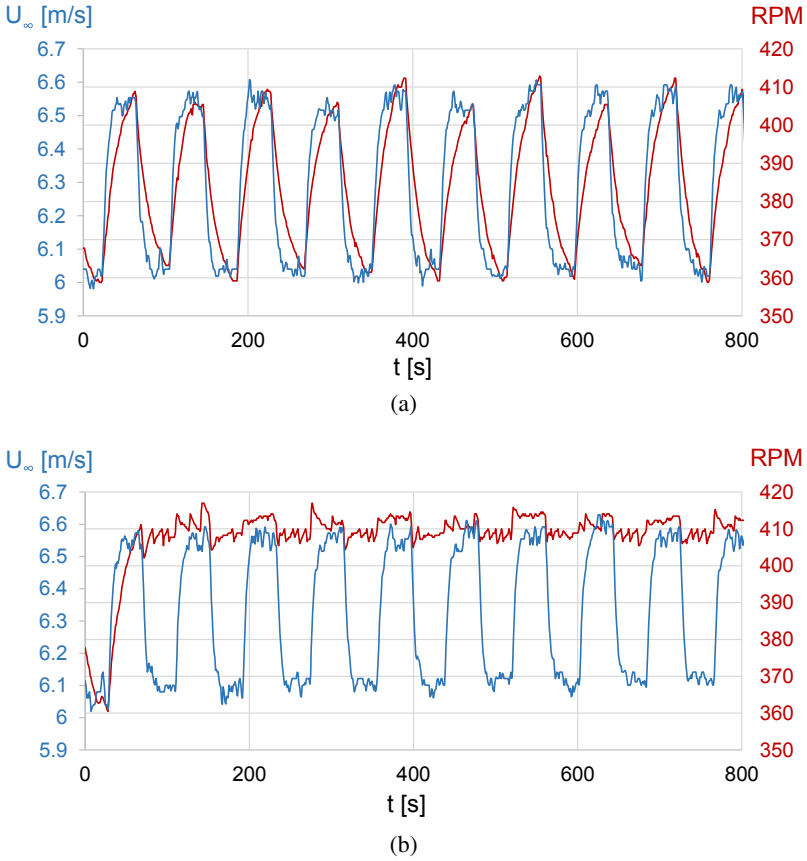

Fig. 11. (a) Wind speed fluctuations shown for a 40 second period together with turbine RPM, proportional to output power: for (a) the uncontrolled, no plasma actuation case, and (b) the feedback control scheme illustrated in fig. 10

The same wind fluctuation profile is shown in fig. 11b, but here feedback control is implemented with RPM_{set} =410. Initiation of control at t=70s produces a response similar to a step function input to the first-order system. Indeed, a linearized first-order model can easily be implement into the feedback control scheme but was not done during these preliminary experiments. After a steady state has been reached, the turbine RPM and, therefore, power fluctuations are dramatically reduced to ±1.3%. Moreover, the mean net turbine power is approximately 7% higher than in the uncontrolled case. A potential improvement to the present setup would be to replace the feed-forward control with a feedback scheme. This could be achieved, for example, by placing sensors on the blade surface with the purpose of sensing unsteady separation or incipient dynamic stall. An alternative would be to use adaptive control based on instantaneous measurements of turbine power, thus eliminating the need for wind speed (and direction) measurements.

6 Conclusions

This paper summarized our recent results relating to the use of DBD plasma actuators as a means for controlling the flow, and hence the power and loads, on a 2-bladed vertical axis wind turbine. Open-loop control, feed-forward control and combined feed-forward/feedback control schemes were considered.

Baseline PIV data showed a large dynamic stall vortex in the process of being shed from the blade. With actuation applied in an open-loop manner, the vortex was smaller and closer to the surface. At lower maximum angles-of-attack the effect of pulsations on the dynamic stall was greater, but separation was not fully controlled.

Feed-forward perturbations were effective at increasing turbine power when applied at angles significantly larger than the static stall angle, in the approximate range $23° \le \alpha \le 35°$. Furthermore, successively reducing the active azimuthal angle range and reducing the pulsations duty cycles produced a net positive turbine power increase of 10%. Thus feed-forward control was consistently superior to open-loop control due to the reduced turbine duty cycle and elimination of the adverse effect of actuation under pre-stall conditions.

Feedback (hysteresis) control resulted in a reduction in turbine power fluctuations from ±6.5% to ±1.3% and a mean power increase of 7%. Potential improvements to the present control scheme include a dynamical model of the turbine and replacement of the feed-forward control by feedback control based on sensors on the turbine blade and/or adaptive control based on instantaneous measurements of turbine power.

References

1. MacPhee, D., Beyene, A.: Recent Advances in Rotor Design of Vertical Axis Wind Turbines. Wind Engineering 36(6), 647–666 (2012)
2. Islam, M., Ting, D.S.-K., Fartaj, A.: Aerodynamic models for Darrieus-type straight-bladed vertical axis wind turbines. Renewable and Sustainable Energy Reviews 12, 1087–1109 (2008)

3. Howell, R., Qin, N., Edwards, J., Durrani, N.: Wind tunnel and numerical study of a small vertical axis wind turbine. Renewable Energy 35, 412–422 (2010)
4. McLaren, K., Tullis, S., Ziada, S.: Computational fluid dynamics simulation of the aerodynamics of a high solidity, small-scale vertical axis wind turbine. Wind Energy 15, 349–361 (2012)
5. Scheurich, F., Fletcher, T.M., Brown, R.E.: Simulating the aerodynamic performance and wake dynamics of a vertical-axis wind turbine. Wind Energy 14, 159–177 (2011)
6. Marsh, G.: Offshore reliability. Renewable Energy Focus, 62–65 (May/June 2012)
7. Shires, A.: Design optimisation of an offshore vertical axis wind turbine. Energy 166(1), 7–18, Proceedings of the Institution of Civil Engineers, doi.org/10.1680/ener.12.00007.
8. Akimoto, H., Tanaka, K., Uzawa, K.: Floating axis wind turbines for offshore power generation – a conceptual study. Environmental Research Letters 6(4), 044017 (2011), doi:10.1088/1748-9326/6/4/044017
9. Carr, L.W.: Progress in the analysis and prediction of dynamic stall. AIAA Journal of Aircraft 25(1), 6–17 (1988)
10. Simão Ferreira, C.J., van Zuijlen, A., Bijl, H., van Bussel, G.J.W., van Kuik, G.A.M.: Simulating dynamic stall in a two-dimensional vertical-axis wind turbine: Verification and validation with particle image velocimetry data. Wind Energy 13(1), 1–17 (2009)
11. Simão Ferreira, C.J., van Kuik, G.A.M., van Bussel, G.J.W., Scarano, F.: Visualization by PIV of dynamic stall on a vertical axis wind turbine. Experiments in Fluids 46(1), 97–108 (2009)
12. Paraschivoiu, I.: Double-multiple streamtube model for Darrieus wind turbines. In: Second DOE/NASA Wind Turbines Dynamics Workshop, NASA CP-2186, Cleveland, OH, pp. 19–25 (February 1981)
13. Greenblatt, D., Neuburger, D., Wygnanski, I.: Dynamic Stall Control by Intermittent Periodic Excitation. AIAA Journal of Aircraft 38(1), 188–190 (2001)
14. Greenblatt, D., Wygnanski, I.: Dynamic stall control by periodic excitation. Part 1: NACA 0015 Parametric Study. AIAA Journal of Aircraft 38(3), 430–438 (2001)
15. Greenblatt, D.: Active Control of Leading-Edge Dynamic Stall. International Journal of Flow Control 2(1), 21–38 (2010)
16. Greenblatt, D., Wygnanski, I.: The control of separation by periodic excitation. Progress in Aerospace Sciences 36(7), 487–545 (2000)
17. Post, M.L., Corke, T.C.: Separation control using plasma actuators: dynamic stall vortex control on oscillating airfoil. AIAA Journal 44, 3125–3135 (2006)
18. Greenblatt, D., Schulman, M., Ben-Harav, A.: Vertical axis wind turbine performance enhancement using plasma actuators. Renewable Energy 37(1), 345–354 (2012)
19. Greenblatt, D., Ben-Harav, A., Mueller-Vahl, H.: Dynamic Stall Control on a Vertical-Axis Wind Turbine Using Plasma Actuators. AIAA Journal 52(2), 456–462 (2014), doi:10.2514/1.J052776.
20. Corke, T.C., Post, M.L., Orlov, D.M.: SDBD Plasma Enhanced Aerodynamics: Concepts, Optimization and Applications. Progress in Aerospace Sciences 43, 193–217 (2007)
21. Müller-Vahl, H., Strangfeld, C., Nayeri, C.N., Paschereit, C.O., Greenblatt, D.: Thick Airfoil Dynamic Stall. In: Euromech Colloquium 528 “Wind Energy and the Impact of Turbulence on the Conversion Process. Springer (2013) (in press)
22. Attinello, J.S.: Design and engineering features of flap blowing installations. In: Lachmann, G.V. (ed.) Boundary Layer and Flow Control. Its Principles and Application, vol. 1, pp. 463–515. Pergamon Press, New York (1961)

23. Thomas, F.O., Corke, T.C., Iqbal, M., Kozlov, A., Schatzman, D.: Optimization of Dielectric Barrier Discharge Plasma Actuators for Active Aerodynamic Flow Control. AIAA Journal 47(9), 2169–2178 (2009)
24. Greenblatt, D., Göksel, B., Rechenberg, I., Schüle, C., Romann, D., Paschereit, C.O.: Dielectric Barrier Discharge Flow Control at Very Low Flight Reynolds Numbers. AIAA Journal 46(6), 1528–1541 (2008)
25. Furman, Y., Müller-Vahl, H., Greenblatt, D.: Development of a Low-Speed Oscillatory Flow Wind Tunnel. In: 51st AIAA Aerospace Sciences Meeting, Grapevine, Texas, AIAA Paper 2013-0505 (2013)
26. Göksel, B., Greenblatt, D., Rechenberg, I., Nayeri, C.N., Paschereit, C.O.: Steady and Unsteady Plasma Wall Jets for Separation and Circulation Control. In: 3rd AIAA Flow Control Conference, San Francisco, California, USA, June 5-8, AIAA Paper 2006-3686 (2006)